



Oxygen-driven bulk defect engineering in carbon to reduce voltage hysteresis for fast potassium storage at low voltage

Zongfu Sun, Yaxin Chen^{*}, Chao Geng, Ying Li, Weijia Guo, Jiangmin Jiang, Yongli Cui, Yueli Shi, Quanchao Zhuang, Zhicheng Ju^{*}

School of Materials Science and Physics, China University of Mining and Technology, Xuzhou 221116, PR China

ARTICLE INFO

Keywords:

Carbon materials
Bulk defect
Voltage hysteresis
Fast kinetics
Potassium-ion batteries

ABSTRACT

Reducing the voltage hysteresis and enhancing the rate performance of carbon anode materials are critical for boosting the energy and power density of potassium-ion full-cell devices. In this study, we report an oxygen-driven bulk defect engineering in carbon to reduce the voltage hysteresis, enabling reversible and fast potassium storage at low voltage. Through high-concentration hydrothermal treatment, the oxidized pitch structure units undergo a process where oxygen bridge bonds are formed, resulting in the creation of interconnected bulk structures. The oxygen-containing functional groups are removed during carbonization, thereby introducing bulk defects into the carbon materials to enhance the kinetics of K^+ insertion in the nanographite domains. The bulk carbon anode achieves low voltage hysteresis, high reversible capacity below 1 V (248 mAh g^{-1} at 0.05 A g^{-1}) and high-rate (192 mAh g^{-1} at 1 A g^{-1}). Additionally, the full cell exhibits a discharge plateau at approximately 3.1 V and high cyclic stability (95 % capacity retention from the 10th to the 120th cycle). This study presents a novel approach for constructing bulk defects in carbon materials to achieve efficient potassium storage at low potential, thus advancing the application of advanced carbon anodes in potassium-ion batteries.

1. Introduction

Potassium-ion batteries (PIBs) have emerged as a promising alternative to lithium-ion batteries (LIBs) due to their comparable properties and potential application in the field of large-scale energy storage [1–3]. Carbon materials have garnered significant research attention as candidate anode materials, owing to their stable physicochemical properties and excellent electrochemical performance [4–6]. However, with the rapid development of green energy, there is a growing need for batteries with both high energy and power density. To address this, enhancing the low potential potassium storage capability of carbon anodes is crucial, as it enables higher output voltage in the overall device and facilitates achieving higher energy density [7,8]. Additionally, achieving excellent rate performance necessitates fast diffusion kinetics of potassium ion (K^+) within the carbon anode, which is essential for attaining higher power density in the complete device [9,10]. Therefore, the development of a novel advanced carbon anode materials to achieve high performance of PIBs that enable fast potassium storage at low voltage is critical but faces challenges.

The potassium storage voltage of carbon materials relies on the

storage behavior of K ion [11]. K^+ are stored through interlayer insertion within the microcrystalline region of the carbon material, leading to the formation of a low voltage plateau and high reversible capacity [12, 13]. As is known, graphite provides a low voltage potassium storage platform at ca. 0.2 V by intercalation with K^+ to form potassium graphite intercalation compounds (K-GICs), which is mainly attribute to the abundant laminate structure [14]. However, the narrow interlayer spacing in graphite results in sluggish diffusion kinetics of K^+ , severely impacting the rate performance [15]. Soft carbon with turbine laminate structure is often considered as a potential alternative to graphite anode materials [16,17]. The intercalation reaction of soft carbon with K^+ forms the KC_8 compound at around 0.14 V, slightly higher than the 0.10 V required for KC_8 formation in graphite, suggesting a more favorable electrochemical process for low voltage potassium storage [18]. Nevertheless, the formation of turbo layers and distorted graphene layer structures in soft carbon increases the resistance to K^+ insertion/de-insertion, resulting in high voltage hysteresis at low voltage and poor rate performance [19]. Therefore, there is an urgent need to regulate the microstructure of carbon materials to improve K^+ diffusion kinetics, which is essential for achieving low voltage hysteresis

^{*} Corresponding authors.

E-mail addresses: chenyxcumt@163.com (Y. Chen), juzc@cumt.edu.cn (Z. Ju).

<https://doi.org/10.1016/j.apcatb.2023.123473>

Received 9 August 2023; Received in revised form 6 October 2023; Accepted 5 November 2023

Available online 7 November 2023

0926-3373/© 2023 Elsevier B.V. All rights reserved.

and fast potassium storage at low voltage.

Defect engineering has been considered as an effective approach to improve the diffusion kinetics of K^+ in carbon materials, including introduction pore structure [20], heteroatomic doping [21] and construction of C–C sp^3 defects [22]. The pore structure increases edge defects and shorten the migration path of ions, which improves the rate performance [23]. The doping of heteroatoms expands the layer spacing and provides more active sites for K^+ storage [24]. Besides, the construction of C–C sp^3 defects could produce more pathways for efficient K^+ diffusion [25]. However, these surface defects often lead to a significant number of irreversible reactions during the potassium storage process, resulting in substantial electrolyte consumption [26–28]. Consequently, this leads to a low initial cycle efficiency (ICE) and high potassium storage voltage, which hinders the practical application of PIBs. For instance, N/S dual-doped graphitic carbon with hollow architectures (ICE=17 %) [29], N/O dual-doped carbon nanospheres (ICE=29.3 %) [30], Covalent organic frameworks derived carbon (44.6 %) [31] and oxygen-rich carbon nanosheets (19 %) [32]. Recent studies have focused on the construction of composite carbon materials, which can form passivation layers on surface defects, reducing irreversible reactions and improving ICE [33,34]. However, the presence of a passivated layer often compromises the activity of defects, thus limiting the ion transport pathway and adversely affecting the rate performance of the carbon material [35]. Therefore, developing effective strategies to coordinate K^+ storage sites and diffusion kinetics present a challenge in achieving fast potassium storage at low voltage in carbon materials.

Herein, an oxygen-driven bulk defect engineering is developed to reduce voltage hysteresis in carbon for fast potassium storage at low voltage. The cross-linking of oxidized pitch through the formation of oxygen bridge bonds during high-concentration hydrothermal treatment, as well as the subsequent removal of oxygen-containing functional groups during carbonization, are both crucial in the in-situ construction of bulk defects in carbon materials. The construction of bulk defects provides a fast pathway for the diffusion of potassium ions into the carbon layer, reducing the voltage hysteresis, which enables rapid and reversible potassium storage at low potential. The bulk carbon anode performances low voltage hysteresis, high reversible capacity below 1 V (248 mAh g^{-1} at 0.05 A g^{-1}) and high-rate (192 mAh g^{-1} at 1 A g^{-1}). Moreover, the BC-6 h/KPB full cell shows a significant discharge plateau at ca. 3.1 V and excellent cyclic stability (95 % from cycle 10th to 120th). These findings not only provide insights into the relationship between bulk defects in carbon materials and the potassium ion storage mechanism but also offer valuable ideas for the rational design of advanced carbon anode materials for practical applications of potassium-ion batteries.

2. Experiment

2.1. OPCs, BCs and KPB fabrication

Firstly, coal tar pitch was oxidized by the chemical oxidation reaction at different time (2 h, 6 h, 10 h) for 60 °C in HNO_3 and H_2SO_4 solution. The volume ratio of H_2SO_4 (mass fraction of 98 %) and HNO_3 (mass fraction of 68 %) was 3:1 in a mixed acid solution. The oxidized pitch was collected through centrifugation and then dialyzed into neutral to gain the oxidized pitch solution. The oxidized pitch solution was freeze-dried at –60 °C followed by carbonization at 1100 °C to obtain oxidized pitch-based carbons (OPCs). These samples are denoted as OPC-2 h, OPC-6 h and OPC-10 h, numbered respectively to their oxidation time.

The oxygen-driven bulk defect engineering was further applied to prepare bulk carbons (BCs). The oxidized pitch solution was dried in oven (60 °C for 48 h). Mixing 1 g of dry oxidized pitch (solute) with 20 ml of deionized water (solvent) for cross-linking at hydrothermal treatment (195 °C for 5 h). After washing with deionized water and drying, the resulting powder was carbonized at 1100 °C for 4 h in Ar.

The obtained bulk carbon was named as BC-2 h, BC-6 h and BC-10 h, numbered respectively to their oxidation time.

The Potassium Prussian Blue (KPB) cathode materials were fabricated in an aqueous solution at room temperature through a typical precipitation method [69].

2.2. Characterization

The morphology and structure of the OPCs and BCs were analyzed by scanning electron microscopy (SEM, Hitachi, SU 8220 field emission microscope) and high-resolution transmission electron microscopy (HRTEM, FEI Tecnai G2 F20). X-ray diffraction (XRD, Rigaku UIV, Cu $K\alpha$, $\lambda = 1.54056 \text{ \AA}$) and Raman spectroscopy (collected using a 532 nm laser, ThermoFisher DXR 2) were utilized to investigate the crystal structures of the samples. The Brunauer-Emmett-Teller (BET) method were used to calculate the specific surface areas (SSAs) of the products. The density functional theory (DFT) and small angle X-ray scattering (SAXS) were employed to analyze the pore size distributions (PSDs). The defect structure was tested by electron paramagnetic resonance (EPR, Bruker EMXPLUS) and true density (AccuPyc II 1340). The electronic conductivity of the BCs was tested by FM100GH powder resistivity tester under a test pressure of 2 MPa. The elemental content was examined through X-ray photoelectron spectroscopy (XPS, ESCALAB 250Xi, Thermo Fisher Scientific). In situ Infrared (IR, NEZTSCH STA 449 F5) spectroscopy was employed to track the constituents of escaping gases during carbonization.

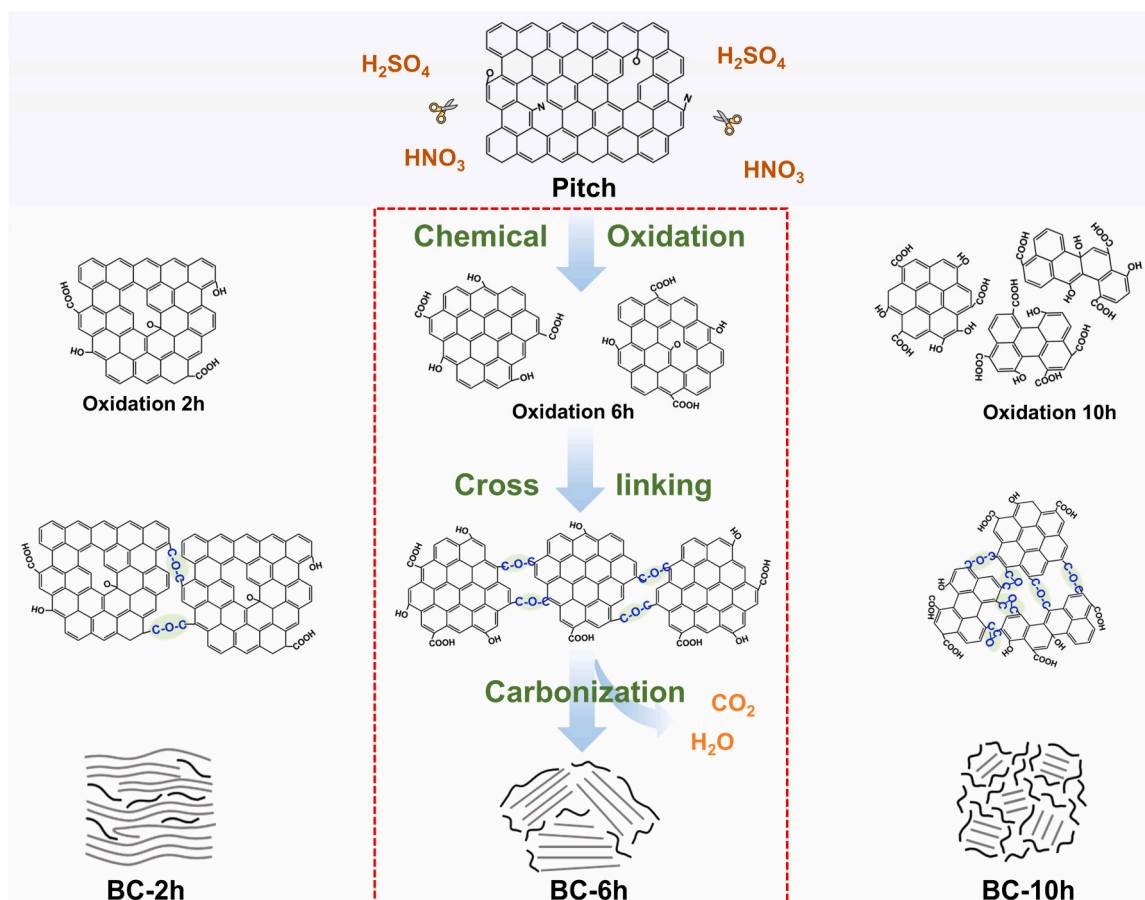
2.3. Electrochemical measurements

The electrochemical performance of the samples was evaluated using CR2025 coin cells. The anode electrodes were prepared by the active material (80 %), acetylene black (10 %) and carboxymethyl cellulose (CMC, 10 %) in deionized water solvent. The cathode electrode was obtained by KPB (80 %), carbon black (10 %) and polyvinylidene fluoride (PVDF, 10 %) in *n*-methyl-2-pyrrolidone (NMP) solvent. The 0.8 mol L^{-1} KPF_6 dissolved in ethylene carbonate (EC) and diethyl carbonate (DEC) (1:1 vol ratio) was used as electrolyte. The separator was glass fiber membrane (Whatman GF/C 47 mm) and the counter electrode was potassium foil. The P/N (cathode/anode) mass ratio in the BC-6 h/KPB full cell was ca. 2:1. The charging and discharging of half-cells at various current densities with potential windows of 0.01–3 V and 2–4.2 V were tests on LAND-T2001A battery tester (Arbin Instruments, BT2043). The galvanostatic intermittent titration technique (GITT) were carried out in the voltage range of 0.01–3 V through the LAND-T2001A battery test system. Cyclic voltammetry (CV) curves and electrochemical impedance spectroscopy (EIS) measurements were obtained in a CHI760D electrochemical workstation (Shanghai Chenhua).

3. Results and discussions

3.1. Synthesis and structural characterization of the BC-2 h, BC-6 h and BC-10 h

The direct pyrolysis of pitch forms a long-range ordered turbo-layered structure, which is unsuitable for rapid potassium storage at low voltage [36,37]. To address this issue, a bulk defect engineering approach is proposed to create ion diffusion channels in carbon materials (Scheme 1, Fig. S1). The oxidation process disrupts the aromatic structure of the pitch, which in turn introduces oxygen-containing functional groups at the edges. Additionally, by prolonging the oxidation time, the pitch molecule undergoes a gradual decrease in thick-ringed aromatic hydrocarbons and an increase in oxygen-containing functional groups. Furthermore, the oxygen-containing functional groups of the oxidized pitch are brought into full contact within a high-concentration solvent, which induces cross-linking and the formation of chemical bonds through the removal



Scheme 1. Schematic diagram of oxygen-driven bulk defect engineering in carbon materials.

of H_2O molecules. Finally, during high-temperature carbonization, chemical bonds with poor thermal stability are broken, generating CO_2 gas and facilitating the in-situ construction of bulk defects. It is worth noting that the degree of cross-linking of oxygen-containing functional groups directly affects the number of bulk defects. By introducing bulk defects in carbon materials, ion transport pathways are created, thereby improving diffusion kinetics and reducing voltage hysteresis.

The oxygen-containing functional groups of oxidized pitch induce cross-linking in a high concentration solution, followed by the broken of chemical bonds during carbonization to form bulk carbons (BCs) with bulk defects. The extent of surface oxidation of oxidized pitch plays a crucial role in the process of cross-linking and the formation of bulk defects. Besides, the aromatic hydrocarbon core of oxidized pitch is equally important for the formation of microcrystalline structures. Firstly, the effect of the oxidation intensity on the microcrystalline structure was investigated after oxidized pitch carbonization. The oxidation process results in uneven etching of the pitch, and with increasing oxidation time, the size of the OPCs gradually reduced from 1 μm to 100 nm (Fig. S2). Fig. 1a-c reveals that prolonging the oxidation time resulted in the reduced size of microcrystalline structure (Fig. S7). Furthermore, the presence of defects in the OPC-2 h, OPC-6 h, and OPC-10 h samples increased with the extent of oxidation (Fig. S3). The (002) diffraction peak of OPCs were fitted, the graphite-like phases of OPC-2 h, OPC-6 h and OPC-10 h account for 51.7 %, 48.6 % and 46.4 % respectively (Fig. S4, S5) [38]. The band intensity ratios of D band to G band (I_D/I_G) of OPC-2 h, OPC-6 h and OPC-10 h are 0.95, 0.97 and 0.99, respectively (Fig. S6). Therefore, the aromatic hydrocarbons of oxidized pitch are controlled by the oxidation time, and in turn regulate the microcrystalline structure during carbonization, which is the basis for achieving potassium storage at low voltage.

An oxygen-driven bulk defect engineering approach was utilized to create ion transport pathways, thereby improving diffusion kinetics and reducing voltage hysteresis at low voltage. As depicted in Fig. 1d-f and S8, the morphology of BC-2 h, BC-6 h, and BC-10 h reveals various sizes of bulk materials. As shown in Fig. 1e and S9, BC-6 h exhibits abundant microcrystalline structures and bulk defects, which facilitate rapid ion diffusion into the microcrystalline regions. However, BC-10 h demonstrates a significant presence of bulk defects while displaying minimal microcrystalline structure (Fig. 1f). Besides, compared to OPC-6 h with small particle size and abundant surface defects, BC-6 h exhibits dense bulk material with few surface defects (Fig. 1g, 1h). As shown in the XRD in Fig. 1i, the three materials all exhibit broad (002) and (100) diffraction peaks. The (002) peak of BC-2 h, BC-6 h and BC-10 h are in the range of $23\text{--}24^\circ$. According to the Bragg equation the layer spacing of products is ca. 0.37–0.38 nm, which is significantly larger than that of graphite (0.335 nm). As depicted in the Raman in Fig. 1j, the I_D/I_G values of BC-2 h, BC-6 h and BC-10 h are 0.93, 0.92 and 1.01, respectively. BC-2 h and BC-6 h display similar degrees of structural order, while BC-10 h presents the highest degree of disorder.

The transformation of the bulk defects in these products were investigated by electron paramagnetic resonance (EPR), small angle X-ray scattering (SAXS) and true density. As shown in Fig. 2a, the Brunauer-Emmett-Teller surface area (S_{BET}) of BC-2 h, BC-6 h and BC-10 h are 245.5, 686.7 and 848.2 $\text{m}^2 \text{g}^{-1}$, respectively. The peak intensities of the Lorentz lines of BC-2 h, BC-6 h and BC-10 h are sequentially enhanced in the EPR spectra (Fig. 2c). The increase in S_{BET} and peak intensity of EPR can be attributed to the release of gases during carbonization, which leads to the formation of bulk defects [39]. As shown in Fig. 2d-f and S10, the SAXS pattern of BC-6 h exhibits the broadest humps around the scattering vector (Q) of 0.1 \AA^{-1} ,

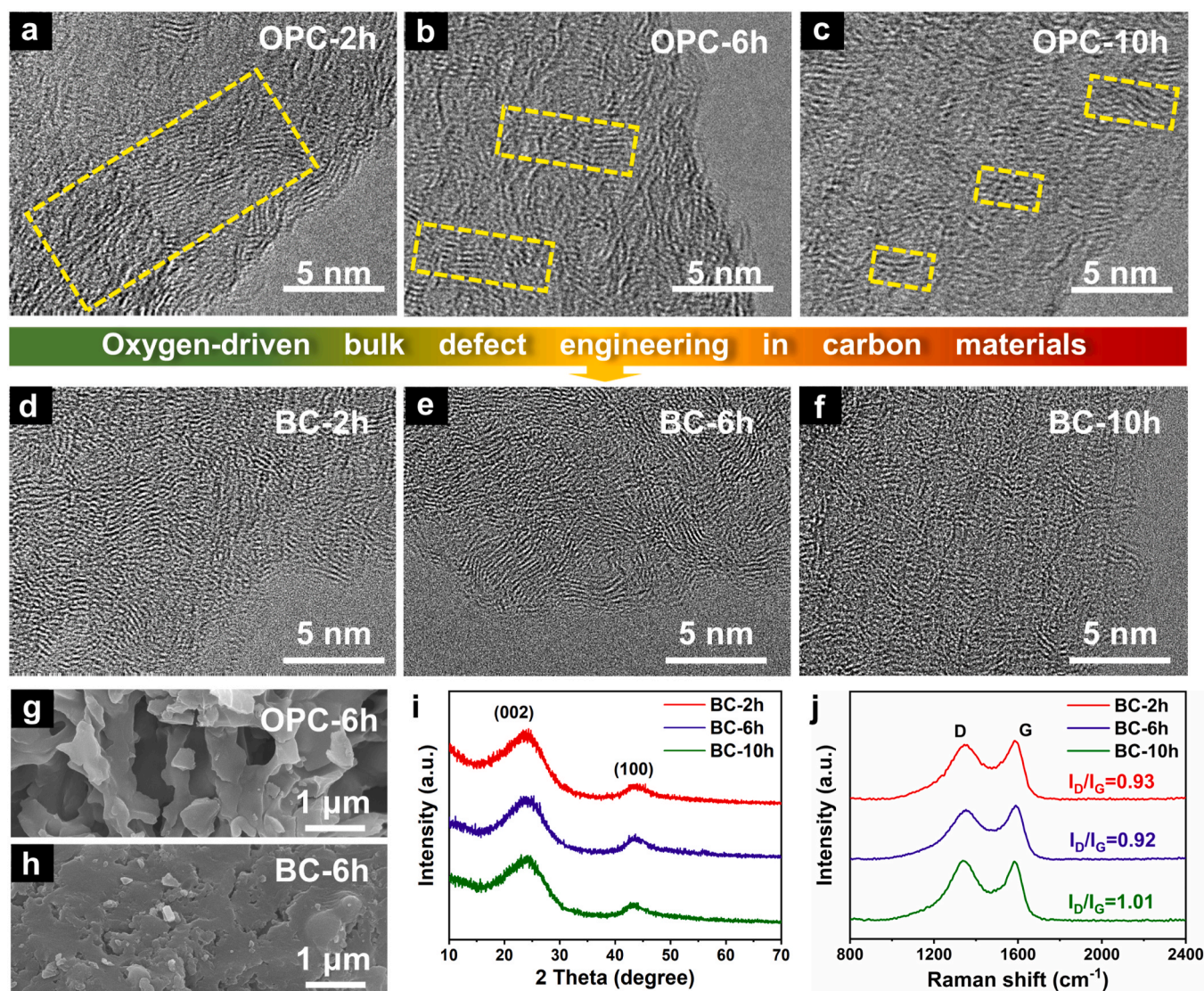


Fig. 1. HRTEM images of (a-c) OPCs and (d-f) BCs. SEM images of (g) OPC-6 h and (h) BC-6 h. (i) XRD patterns and (j) Raman spectra of BC-2 h, BC-6 h and BC-10 h.

demonstrating that the BC-6 h sample possesses the most developed defect structure (surface and bulk defects) [40]. The N_2 adsorption-desorption and SAXS techniques demonstrate the presence of meso- and micropores in BCs (Figs. 2b, 2d-f and S11). It is worth noting that the closed pore specific surface areas of BC-2 h, BC-6 h and BC-10 h are 335.4, 748.02 and 373.26 $m^2 g^{-1}$ respectively, which were obtained by SAXS surface areas minus the S_{BET} . Moreover, the true density of BC-2 h, BC-6 h, and BC-10 h was measured to be 2.13, 2.05, and 1.56 $g cm^{-3}$, respectively (Table 1). From this, the closed pore volume of BC-6 h was calculated to be 0.045 $cm^3 g^{-1}$. Thus, by integrating nitrogen adsorption-desorption data and small-angle X-ray scattering (SAXS) data, it is indicated that BC-6 h exhibits the most developed bulk defect structure. Besides, the intrinsic conductivity of BC-6 h ($42E+03 S m^{-1}$) is higher than that of BC-2 h ($36E+03 S m^{-1}$) and BC-10 h ($18E+03 S m^{-1}$), which could benefit the electron transport during potassium storage (Table 1). In conclusion, BC-6 h possesses a significant abundance of bulk defects, which facilitates the rapid diffusion of K^+ into the microcrystalline structure. This characteristic plays a crucial role in enabling rapid potassium storage at low voltage.

The construction of bulk defects was further investigated by X-ray photoelectron spectra (XPS). The oxygen content in the oxidized pitch molecules was measured to be 22.11 %, 27.53 %, and 32.11 % after 2 h, 6 h, and 10 h of oxidation, respectively, indicating that a higher degree

of oxidation introduces more oxygen-containing functional groups into the carbon material (Fig. S12). The oxygen content of the oxidized pitch decreases after cross-linking reactions in a high concentration solution, primarily due to the removal of H_2O , CO and CO_2 during the cross-linking process to form chemical bonds (Table S1) [41]. As depicted in Fig. 2g-i, the oxidized pitch primarily consists of C-O bonds and C=O bonds resulting from cross-linking. Following the carbonation process, the oxygen content in BC-2 h, BC-6 h, and BC-10 h decreases to 6.5 %, 7.8 %, and 5.8 %, respectively (Fig. S13). The C-O and C=O diffraction peaks observed in BC-2 h, BC-6 h, and BC-10 h undergo significant reduction due to the low binding energy of the carbon-oxygen bond, which easily breaks to generate gas during carbonation.

In situ infrared (IR) spectroscopy was employed to track the constituents of escaping gases during carbonization (Fig. 2j-l and S14). The bulk carbon releases gases such as CO_2 ($550-800 cm^{-1}$, $2150-2420 cm^{-1}$, $3450-3780 cm^{-1}$), CO ($2040-2200 cm^{-1}$), and undergoes the removal of H_2O during the carbonization stage [42]. These gases mainly arise from the decomposition of oxygen-containing functional groups with low thermal stability during carbonization. Importantly, the extent of cross-linking in the bulk carbons directly influences the quantity of gas generated during the carbonization process. As shown in Fig. 2l, BC-10 h generates a significantly higher amount of gas compared to BC-2 h and BC-6 h. The BC-10 h continually produces CO_2

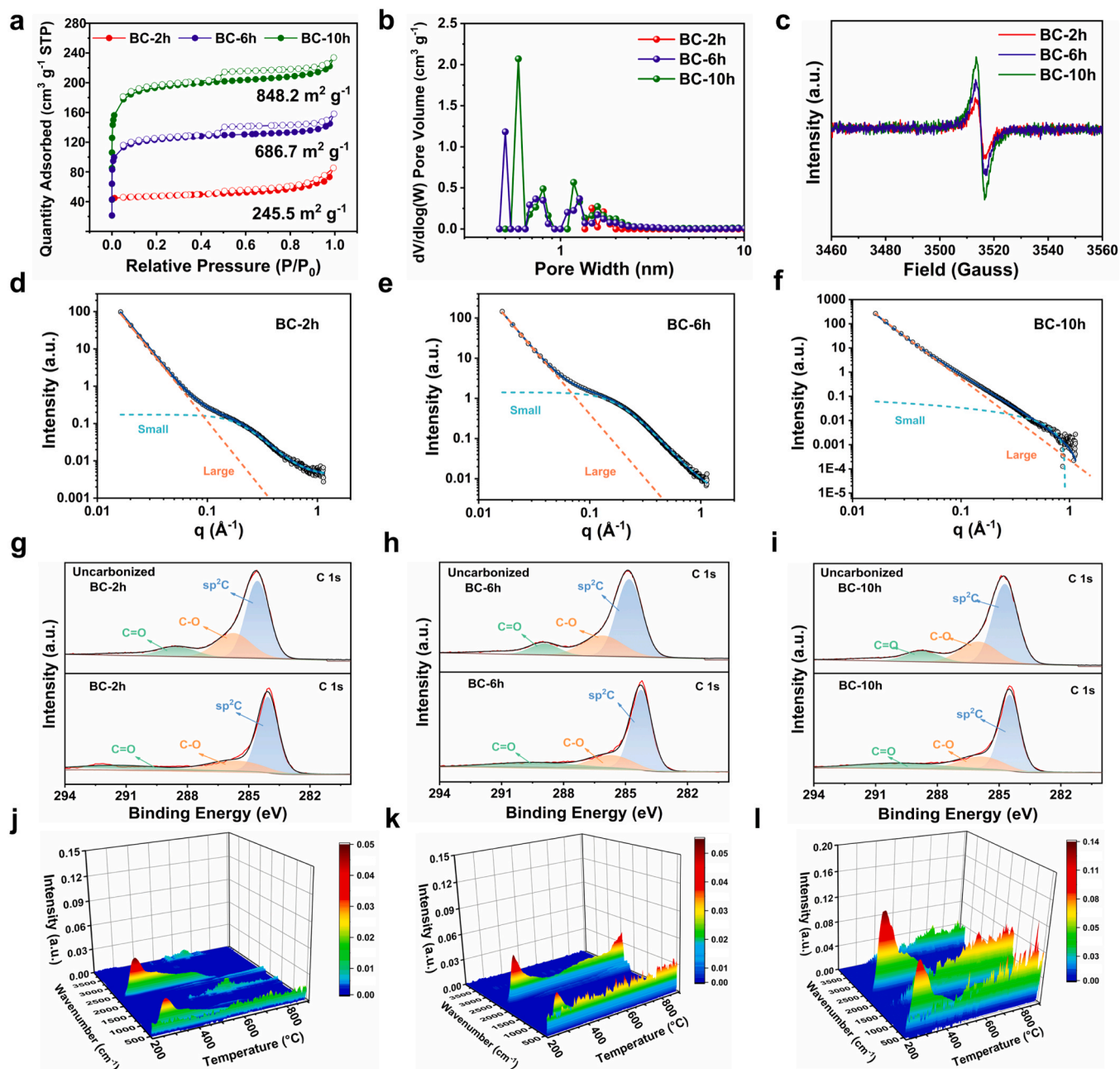


Fig. 2. (a) N₂ adsorption/desorption isotherms, (b) pore size distribution curves, (c) EPR spectra, (d-f) SAXS patterns presenting pores of BC-2 h, BC-6 h and BC-10 h. The high-resolution C 1s spectra of (g) BC-2 h, (h) BC-6 h, (i) BC-10 h before and after carbonization. In situ IR spectra of (j) BC-2 h, (k) BC-6 h and (l) BC-10 h.

Table 1

Pore size information of BC-2 h, BC-6 h and BC-10 h.

Sample	S_{BET} (m ² g ⁻¹)	S_{SAXS} (m ² g ⁻¹)	S_{Closed} pores (m ² g ⁻¹)	V_{Closed} pores (cm ³ g ⁻¹)	True density (g cm ⁻³)	Conductivity (10 ³ S m ⁻¹)
BC-2 h	245.5	580.9	335.4	0.027	2.13	36
BC-6 h	686.7	1434.72	748.02	0.045	2.05	42
BC-10 h	848.2	1221.46	373.26	0.198	1.56	18

gas throughout the carbonation process, demonstrating that a higher number of oxygen-containing functional groups and cross-linked chemical bonds are broken down, resulting in the formation of excess defects. These findings emphasize that the cross-linking of

oxygen-bridging bonds during high-concentration hydrothermal treatment and the disruption of chemical bonds during carbonization play a pivotal role in the in-situ formation of bulk defects in carbon materials. Consequently, oxygen-driven bulk defect engineering enables fast ion diffusion and electron conduction, which are crucial for fast potassium insertion at low voltage.

3.2. Electrochemical performance of the BC-2 h, BC-6 h and BC-10 h

The electrochemical performance of OPCs and BCs were evaluated in half cells with KPF₆ as the electrolyte. The initial coulomb efficiency (ICE) of OPC-6 h (54 %) is higher than that of OPC-2 h (45 %) and OPC-10 h (22 %, Fig. S15). It is evident that proper regulation of the microcrystal structure can enhance the ability for potassium storage at low potential and improve the ICE. However, the presence of disordered

surface defects surrounding the microcrystalline structure hampers the migration of K^+ , leading to increased voltage hysteresis, which ultimately affects the performance at low voltage (Fig. 3a-c and S16, S17). The surface defects are further transformed into bulk defects by oxygen-driven cross-linking behavior. The initial irreversible reactions of BC-2 h, BC-6 h and BC-10 h were reduced compared to OPC-2 h, OPC-6 h and OPC-10 h (Fig. 3d-f). As shown in Fig. S18 and S19, the ICE of BC-2 h, BC-6 h and BC-10 h are 54 %, 65 % and 35 %, respectively, which is attributed to the fact that the large size of the bulk material exposes fewer defects on the surface. Moreover, the curves of the second and third cycles almost overlap, indicating the high reversibility of the BC-2 h, BC-6 h and BC-10 h [43,44]. Importantly, BC-6 h demonstrates significantly smaller voltage hysteresis than BC-2 h and BC-10 h during cycling, thereby effectively enhancing the reversible capacity at low potential (Fig. 3g-i and S20). Moreover, the low voltage hysteresis of BC-6 h exhibits a tremendous advantage compared to the already reported carbon materials (Fig. S21). The reduction in voltage hysteresis can be attributed to the introduction of bulk defects, which effectively reduces irreversible reactions and improves the diffusion kinetics of K^+ at low voltage.

As illustrated in Fig. 4a, the discharge/charge capacities of BC-2 h, BC-6 h and BC-10 h electrodes at 5th cycle are 319.7/285.9, 377.2/344.6 and 265.9/237.3 mAh g^{-1} , respectively. The differential capacity curve (dQ/dV) of the BC-6 h exhibits a distinct oxidation peak at 0.25 V during the charging process, which is lower than that of BC-2 h (0.33 V)

and BC-10 h (0.36 V) (Fig. 4b). This indicates that the BC-6 h possesses a lower voltage hysteresis compared to the BC-2 h and BC-10 h. Fig. 4c demonstrates that the BC-6 h exhibits a high charge capacity of 316.6 mAh g^{-1} after 100 cycles, with a capacity retention of 90.8 % relative to the first cycle. In contrast, the charge capacities of the BC-2 h and BC-10 h after 100 cycles are 263.2 and 236.3 mAh g^{-1} , with capacity retentions of 80.5 % and 79.2 %, respectively. The long-term cyclic stability of the BC-6 h at 1 A g^{-1} is shown in Fig. 4d, where it maintains a charge capacity of 178.6 mAh g^{-1} after 2000 cycles, outperforming the BC-2 h (23.5 mAh g^{-1}) and BC-10 h (51.6 mAh g^{-1}) electrodes. Moreover, the coulombic efficiency of BC-2 h, BC-6 h and BC-10 h are 99.43 %, 99.98 % and 99.61 % during the long-term cycling process. The rate performance of BC-6 h electrode was evaluated when the current density was increased from 0.05 to 1.0 A g^{-1} (Fig. 4e and S22). BC-6 h possesses the charge capacities of ca. 358, 326, 283, 230 and 192 mAh g^{-1} at 0.05, 0.1, 0.2, 0.5 and 1.0 A g^{-1} , respectively. The rate performance of the BC-6 h electrode is noticeably superior to that of a previously reported carbon material (Fig. 4f) [32,45–50]. This improvement can be primarily attributed to the presence of abundant bulk defects, which provide a fast pathway for facilitating the reversible diffusion of K^+ .

To achieve a high output voltage in the device, it is crucial to enhance the reversible capacity of carbon anode materials at low voltage. Therefore, the potassium storage characteristics below 1 V of BC-2 h, BC-6 h, and BC-10 h were further investigated. In the voltage

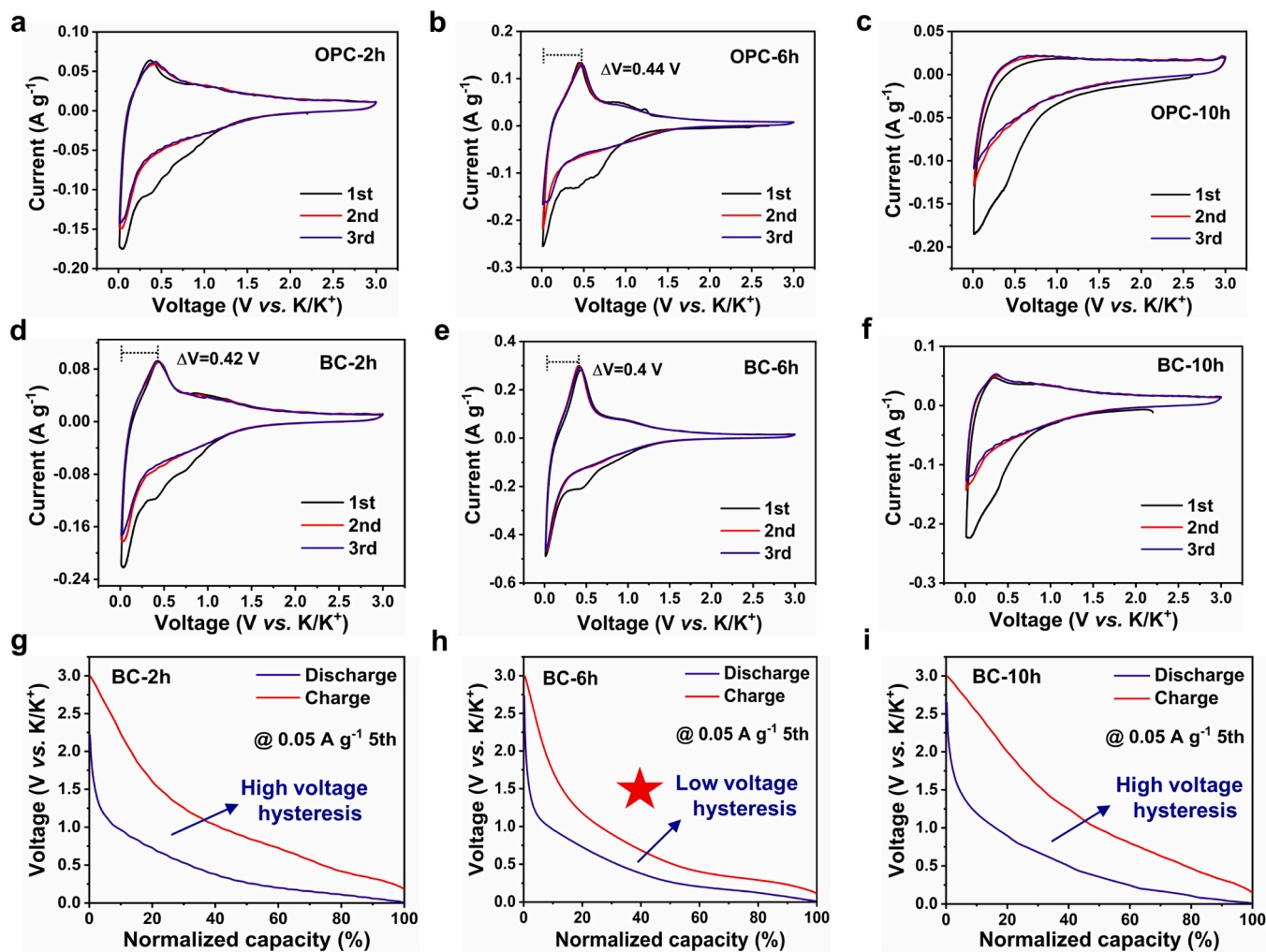


Fig. 3. CV curves of (a) OPC-2 h, (b) OPC-6 h, (c) OPC-10 h, (d) BC-2 h, (e) BC-6 h and (f) BC-10 h at 0.1 mV s^{-1} . The 5th GCD curves of (g) BC-2 h, (h) BC-6 h and (i) BC-10 h at 0.05 A g^{-1} .

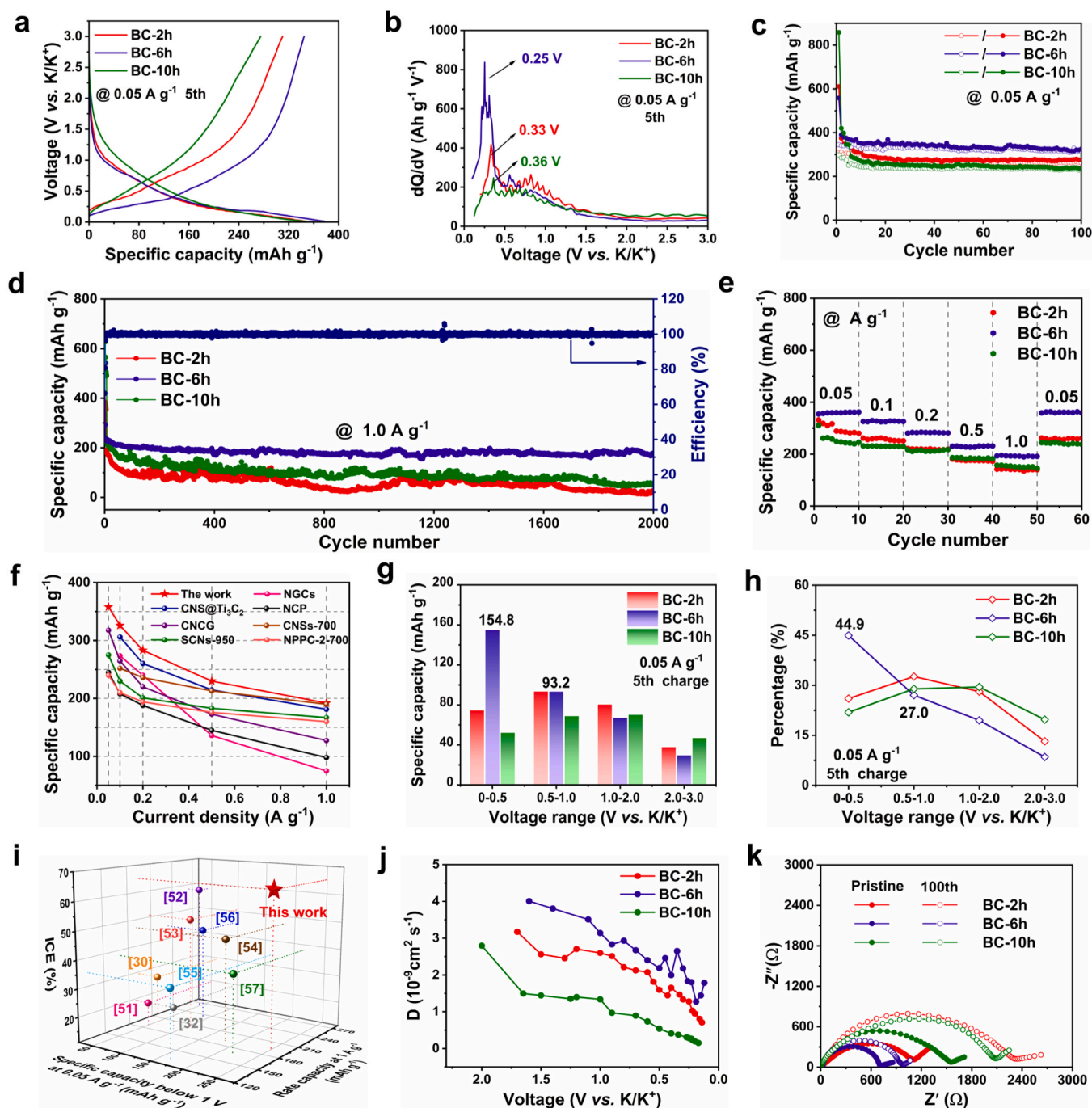


Fig. 4. (a) The 5th GCD curves and (b) dQ/dV curves. Cycling performance at (c) 0.05 A g⁻¹ and (e) 1.0 A g⁻¹. (d) Rate performance and (f) Comparison chart. (g) Quantitative capacities and (h) capacity percentages of different voltage zones. (i) Comparison of ICE, specific capacity below 1 V at 0.05 A g⁻¹ and rate capacity at 1 A g⁻¹ of BC-6 h and other reported carbon materials. (j) K⁺ diffusion coefficient. (k) The Nyquist plots of BC-2h, BC-6 h and BC-10h before cycling and after 100 cycles.

range of 0.01–1 V, BC-6 h exhibited a higher discharge capacity of 354.1 mAh g⁻¹ compared to BC-2 h (292.6 mAh g⁻¹) and BC-10 h (223.8 mAh g⁻¹) at a current density of 0.05 A g⁻¹, as shown in Fig. S23. The discharge capacity percentage of BC-6 h (93.9 %) was close to that of BC-2 h (91.5 %) and BC-10 h (84.2 %) within this voltage range. However, during charging, BC-6 h demonstrated a significantly higher charge capacity of 248 mAh g⁻¹, surpassing BC-2 h (167.7 mAh g⁻¹) and BC-10 h (120.7 mAh g⁻¹) within the 0.01–1 V voltage range, as shown in Fig. 4g. Notably, BC-6 h achieved a still high charge capacity of 154.8 mAh g⁻¹ below 0.5 V, which accounted for 44.9 % of the total charge capacity (Fig. 4h). The charging capacity of BC-2 h is primarily

concentrated around 1 V, which can be attributed to the absence of bulk defects that impede the kinetics of potassium ion diffusion. As a result, this leads to a higher voltage hysteresis. In contrast, BC-10 h exhibits high charge capacity mainly at high voltage, and this can be attributed to the lack of microcrystalline structure. Benefiting from the structure of abundant bulk defects, BC-6 h permits rapid diffusion of K⁺ into the microcrystalline region, which exhibits an extremely promising potassium storage ability at low voltage (Fig. 4i, Table S2) [30,32,51–57].

As shown in Fig. S24, the CV measurements were carried out at various scanning rates from 0.2 mV s⁻¹ to 1.6 mV s⁻¹ to study the K⁺ storage behavior of BC-6 h. It is calculated that the b-value is 0.65 for

BC-2 h, 0.61 for BC-6 h and 0.79 for BC-10 h (Fig. S25). The results indicate that the potassium storage behavior of BC-2 h and BC-6 h is dominated by diffusion, and the potassium storage behavior of BC-10 h is dominated by capacitive control [58]. Besides, the percentage of diffusion contribution of BC-6 h at different sweep speeds is higher than that of BC-2 h and BC-10 h (Fig. S26). The galvanostatic intermittent titration technique (GITT) was employed to calculate the K^+ diffusion coefficient of the electrodes (Fig. S27 and S28). Fig. 4j shows that the diffusion coefficient of the electrodes generally decreases during the discharge process, with BC-6 h exhibiting the highest diffusion coefficient. The electrochemical impedance spectroscopy (EIS) was applied to evaluate the electrochemical kinetics of the electrodes, as shown in Fig. 4k. The BC-6 h displays a much smaller semicircle diameter than the BC-2 h and BC-10 h electrodes. The slight increase of the semicircle diameter after 100 cycles, which is favorable to improve the charge transfer kinetics [59]. It can be ascribed to the construction of bulk defects which is beneficial for the transport of both K^+ and electrons.

3.3. Potassium storage mechanisms of BC-2 h, BC-6 h and BC-10 h

As illustrated in Fig. 5, the relationship between structure and electrochemical performance is constructed to explicate the potassium storage mechanism [60,61]. The modulation of the carbon structure through oxygen-driven bulk defect engineering plays a crucial role in achieving efficient potassium storage at low voltage. It further shortens the microcrystalline structure while promoting the formation of bulk defects. The nanographitic domains with larger layer distance are vital for achieving potassium insertion at low voltage. Furthermore, the introduction of defect structures as ion transport channels is crucial for improving diffusion kinetics. However, surface defects primarily exhibit adsorption-dominated potassium storage behavior, leading to sloping electrochemical curves and high voltage hysteresis. By undergoing

cross-linking reactions of oxygen-containing functional groups, surface defects can be further transformed into bulk defects. This transformation serves to reduce voltage hysteresis and enhance K^+ diffusion kinetics. Benefiting from the fast K^+ diffusion kinetics and low voltage hysteresis, BC-6 h achieves high reversible capacity at low voltage, excellent rate performance and outstanding cycling stability.

3.4. Evaluation of full-cell performance

To evaluate the practical potential of BC-6 h, the PIB full cell device was assembled with KPB cathode [57] and BC-6 h anode (Fig. 6a). As shown in Fig. 6b, the KPB cathode exhibits a discharge plateau around 3.2 V in the range of 2–4.2 V. The BC-6 h//KPB full cell can still maintain the working platform at ca. 3.1 V. In the 2nd cycle, the BC-6 h//KPB full cell exhibits a discharge capacity of 186 mAh g⁻¹ (based on anode mass), corresponding to an energy density of 154 Wh kg⁻¹ (based on cathode and anode mass). The galvanostatic charge-discharge (GCD) curve during cycling shows that the voltage plateau can be maintained, indicating excellent cycle reversibility of the full cell (Fig. S29). Furthermore, the BC-6 h//KPB full cell demonstrates remarkable long-term cyclic stability, with a high capacity retention of 95 % from the 10th to 120th cycles and a high coulombic efficiency (CE) of approximately 98 % during cycling (Fig. 6d). The BC-6 h//KPB full cell also exhibits outstanding rate performance, maintaining discharge capacities of approximately 180.1, 170.5, 155.4, 146.2, 136.8, and 126.1 mAh g⁻¹ at current densities of 0.1, 0.2, 0.3, 0.4, 0.5, and 0.6 A g⁻¹, respectively (Fig. 6c). The curves for BC-6 h//KPB full cell still exhibits significant discharge plateaus at different current densities. In summary, the excellent electrochemical properties of the BC-6 h anode make the BC-6 h//KPB full cell promising for practical applications (Fig. 6e) [62–68].

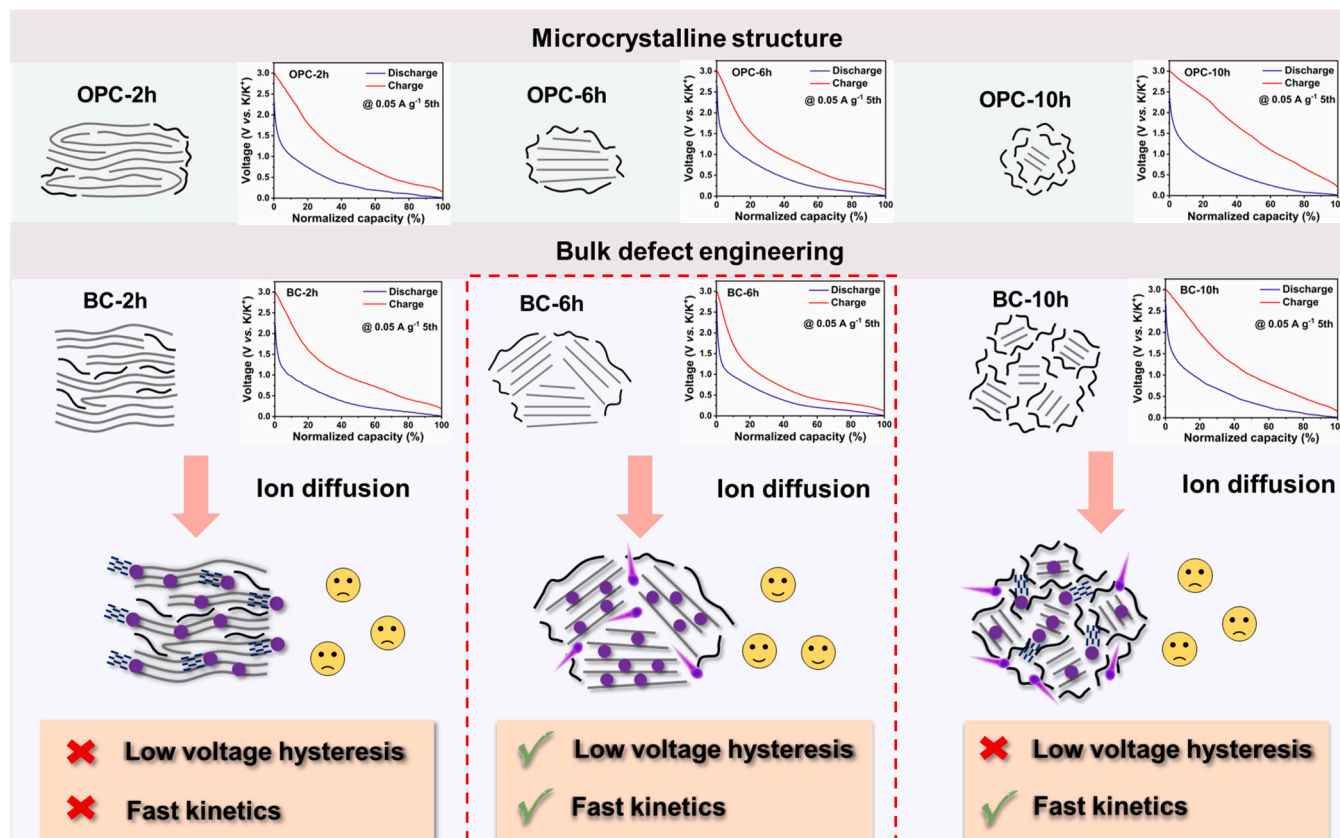


Fig. 5. Schematic illustration of the potassium storage mechanism in BC-2 h, BC-6 h and BC-10 h.

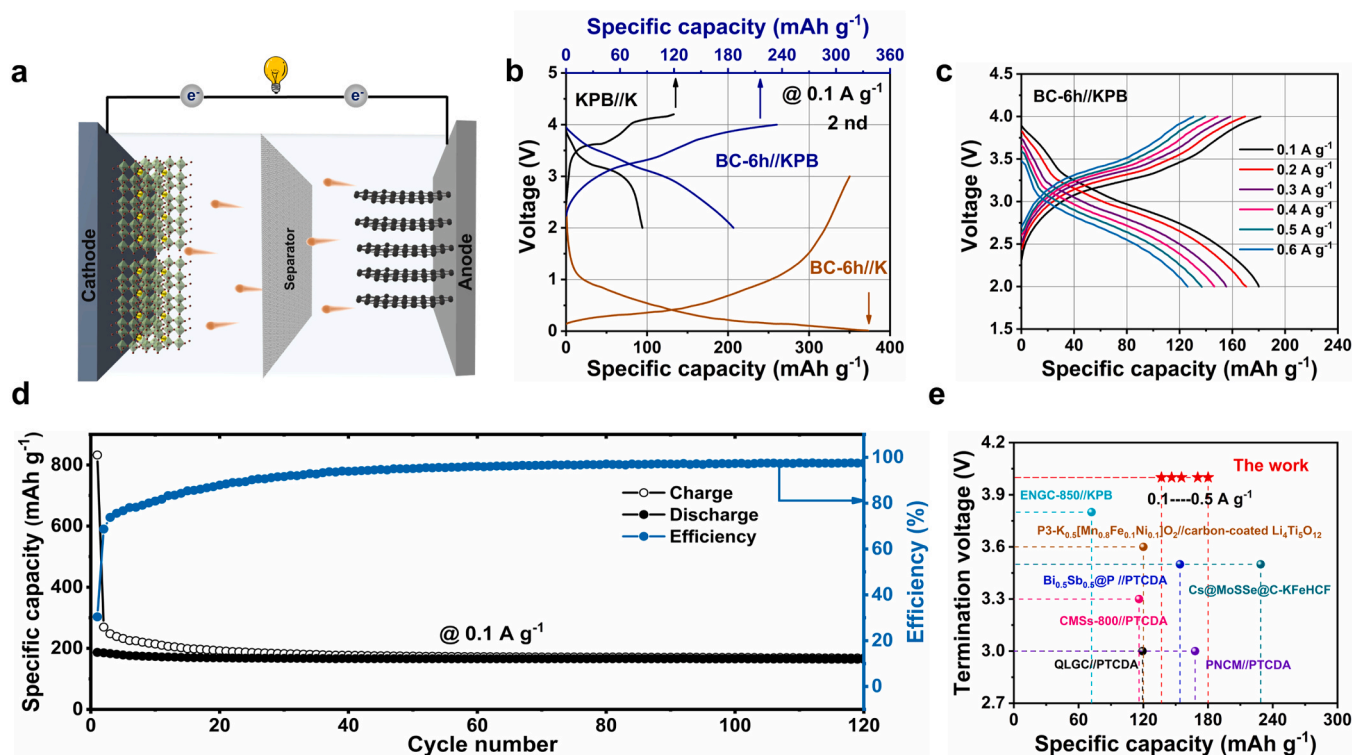


Fig. 6. Electrochemical performance of the BC-6 h//KPB full cell: (a) Schematic illustration of the full cell during discharging. (b) Typical GCD curves of KPB cathode, BC-6 h anode and BC-6 h//KPB full cell. (c) Rate performance of the full cell at different current densities. (d) The long cycling performance of the full cell at 0.1 A g⁻¹. (e) Comparison of electrochemical performances for the BC-6 h//KPB full cell.

4. Conclusions

In summary, an oxygen-driven bulk defect engineering was reported to reduce voltage hysteresis in carbon for fast potassium storage at low voltage. The oxygen-driven cross-linking of the oxidized pitch in high concentration hydrothermal treatment and the broken of chemical bonds during carbonization were demonstrated to be the key to construction the bulk defect of carbon materials. The bulk defect around microcrystalline structures ensure fast rapid diffusion kinetics of K⁺ reversible intercalation, which facilitates the reduction of voltage hysteresis and achieves fast potassium storage. Compared to previously reported carbon materials, BC-6 h exhibits low voltage hysteresis, high reversible capacity below 1 V (248 mAh g⁻¹ at 0.05 A g⁻¹), high-rate (192 mAh g⁻¹ at 1 A g⁻¹) and superior cyclic stability (93 % in 1000 cycles). More importantly, the BC-6 h//KPB full cell provides a significant discharge plateau at ca. 3.1 V and excellent cyclic stability (95 % from cycle 10th to 120th). Kinetic and potassium storage mechanism analysis indicates that the construction of bulk defect not only achieve fast ion diffusion to reduce voltage hysteresis, but also provide fast electron transport to increase reversible capacity at low voltage. This work extensions the thoughts for the fabrication of novel carbon materials for practical application and provides mechanism insights into the bulk defect of carbon materials to promote the fast and reversible K⁺ intercalation.

CRediT authorship contribution statement

Zongfu Sun: Methodology, Validation, Formal analysis, Investigation, Data curation, Writing – original draft. **Yaxin Chen:** Conceptualization, Data curation, Formal analysis, Investigation, Methodology, Writing – review & editing, Supervision, Funding acquisition. **Chao Geng:** Formal analysis, Investigation, Writing – review & editing. **Ying Li:** Formal analysis, Investigation, Writing – review & editing. **Weijia Guo:** Formal analysis, Investigation, Writing – review & editing.

Jiangmin Jiang: Resources, Writing – review & editing. **Yongli Cui:** Resources, Writing – review & editing. **Yueli Shi:** Resources, Writing – review & editing. **Quanchao Zhuang:** Resources, Writing – review & editing. **Zhicheng Ju:** Resources, Supervision, Writing – review & editing, Funding acquisition.

Declaration of Competing Interest

The authors declare that they have no known competing financial interests or personal relationships that could have appeared to influence the work reported in this paper.

Data availability

Data will be made available on request.

Acknowledgements

This research was supported by the National Natural Science Foundation of China (21975283, 22279162), the Natural Science Foundation of Jiangsu Province (Youth Fund, BK20221138). The authors thank the Advanced Analysis & Computation Center of China University of Mining and Technology for the help in material characterization.

Appendix A. Supporting information

Supplementary data associated with this article can be found in the online version at [doi:10.1016/j.apcatb.2023.123473](https://doi.org/10.1016/j.apcatb.2023.123473).

References

- [1] C.-Y. Wang, T. Liu, X.-G. Yang, S.H. Ge, N.V. Stanley, E.S. Rountree, Y.J. Leng, B. D. McCarthy, Fast charging of energy-dense lithium-ion batteries, *Nature* 611 (2022) 485–490, <https://doi.org/10.1038/s41586-022-05281-0>.

- [2] A.M. Bates, Y. Preger, L. Torres-Castro, K.L. Harrison, S.J. Harris, J. Hewson, Are solid-state batteries safer than lithium-ion batteries? *Joule* 6 (2022) 742–755, <https://doi.org/10.1016/j.joule.2022.02.007>.
- [3] M. Winter, B. Barnett, K. Xu, Before li ion batteries, *Chem. Rev.* 118 (2018) 11433–11456, <https://doi.org/10.1021/acs.chemrev.8b00422>.
- [4] X. Wu, Y.L. Chen, Z. Xing, C.W.K. Lam, S.-S. Pang, W. Zhang, Z.C. Ju, Advanced carbon-based anodes for potassium-ion batteries, *Adv. Energy Mater.* 9 (2019), 1900343, <https://doi.org/10.1002/aenm.201900343>.
- [5] W.Y. Long, B.Z. Fang, A. Ignaszak, Z.Z. Wu, Y.-J. Wang, D. Wilkinson, Biomass-derived nanostructured carbons and their composites as anode materials for lithium ion batteries, *Chem. Soc. Rev.* 46 (2017) 7176–7190, <https://doi.org/10.1039/C6CS00639F>.
- [6] L. Chen, D.Y. Zhu, J.T. Li, X.X. Wang, J.F. Zhu, P.S. Francis, Y.H. Zheng, Sulfur and potassium co-doped graphitic carbon nitride for highly enhanced photocatalytic hydrogen evolution, *Appl. Catal. B Environ.* 273 (2020), 119050, <https://doi.org/10.1016/j.apcatb.2020.119050>.
- [7] B. Chen, X.W. Zhong, G.M. Zhou, N.Q. Zhao, H.-M. Cheng, Graphene-supported atomically dispersed metals as bifunctional catalysts for next-generation batteries based on conversion reactions, *Adv. Mater.* 34 (2021), 2105812, <https://doi.org/10.1002/adma.202105812>.
- [8] J.Y. Yang, Y.X. Zhai, X.H. Zhang, E. Zhang, H.Q. Wang, X.R. Liu, F. Xu, S. Kaskel, Perspective on carbon anode materials for K⁺ storage: balancing the intercalation-controlled and surface-driven behavior, *Adv. Energy Mater.* 11 (2021), 2100856, <https://doi.org/10.1002/aenm.202100856>.
- [9] H.N. Xie, B. Chen, C.Y. Liu, G.X. Wu, S.M. Sui, E.Z. Liu, G.M. Zhou, C.N. He, W. B. Hu, N.Q. Zhao, Engineering the interfacial doping of 2D heterostructures with good bidirectional reaction kinetics for durably reversible sodium-ion batteries, *Energy Storage Mater.* 60 (2023), 102830, <https://doi.org/10.1016/j.ensm.2023.102830>.
- [10] Z.L. Pan, T. Zhang, X.F. Qian, Y.X. Zhao, Probing the fast transformation mechanism of Cr (VI) on carbon dots with structural defects and surface oxygen functional groups, *Appl. Catal. B Environ.* 330 (2023), 122571, <https://doi.org/10.1016/j.apcatb.2023.122571>.
- [11] D.H. Wei, J. Yin, Z.C. Ju, S.Y. Zeng, H.B. Li, W. Zhao, Y.Y. Wei, H.Y. Li, Cage-like P₄S₃ molecule as promising anode with high capacity and cycling stability for Li⁺/Na⁺/K⁺ storage, *J. Energy Chem.* 50 (2020) 187–194, <https://doi.org/10.1016/j.ijechem.2020.03.021>.
- [12] X.Y. Lin, J.Q. Huang, B. Zhang, Correlation between the microstructure of carbon materials and their potassium ion storage performance, *Carbon* 143 (2019) 138–146, <https://doi.org/10.1016/j.carbon.2018.11.001>.
- [13] J. Zhao, X.X. Zou, Y.J. Zhu, Y.H. Xu, C.S. Wang, Electrochemical intercalation of potassium into graphite, *Adv. Funct. Mater.* 26 (2016) 8103–8110, <https://doi.org/10.1002/adfm.201602248>.
- [14] Z.L. Jian, W. Luo, X.L. Ji, Carbon electrodes for k-ion batteries, *J. Am. Chem. Soc.* 137 (2015) 11566–11569, <https://doi.org/10.1021/jacs.5b06809>.
- [15] L. Li, L.J. Liu, Z. Hu, Y. Lu, Q.N. Liu, S. Jin, Q. Zhang, S. Zhao, S.L. Chou, Understanding high-rate K⁺-solvent co-intercalation in natural graphite for potassium-ion batteries, *Angew. Chem. Int. Ed.* 59 (2020) 12917–12924, <https://doi.org/10.1002/anie.202001966>.
- [16] S.J. Wu, Y. Song, C.X. Lu, T. Yang, S.X. Yuan, X.D. Tian, Z.J. Liu, An adsorption-insertion mechanism of potassium in soft carbon, *Small* 18 (2022), 2105275, <https://doi.org/10.1002/smll.202105275>.
- [17] M.Y. Ou, Y.P. Zhang, Y.C. Zhu, C.Y. Fan, S.X. Sun, J.T. Feng, X.P. Sun, P. Wei, J. Xu, J. Peng, X.Y. Wu, G. Jiang, Q. Li, C. Fang, J.T. Han, Local structures of soft carbon and electrochemical performance of potassium-ion batteries, *ACS Appl. Mater. Interfaces* 13 (2021) 28261–28269, <https://doi.org/10.1021/acsami.1c06303>.
- [18] Y. Liu, Y.-X. Lu, Y.-S. Xu, Q.-S. Meng, J.-C. Gao, Y.-G. Sun, Y.-S. Hu, B.-B. Chang, C.-T. Liu, A.-M. Cao, Pitch-derived soft carbon as stable anode material for potassium ion batteries, *Adv. Mater.* 32 (2020), 2000505, <https://doi.org/10.1002/adma.202000505>.
- [19] S.J. Wu, Y. Song, C.X. Lu, T. Yang, S.X. Yuan, X.D. Tian, Z.J. Liu, High-rate soft carbon anode in potassium ion batteries: the role of chemical structures of pitches, *Carbon* 203 (2023) 211–220, <https://doi.org/10.1016/j.carbon.2022.11.058>.
- [20] C. Geng, Y.X. Chen, Z.F. Sun, W.J. Guo, J.M. Jiang, Y.L. Cui, Y.L. Shi, Q.C. Zhuang, Z.C. Ju, “Pulverization–Reaggregation”-induced in situ pore expansion in carbon for fast potassium storage, *J. Mater. Chem. A* 10 (2022) 22399–22407, <https://doi.org/10.1039/d2ta04883c>.
- [21] J.L. Yang, Z.C. Ju, Y. Jiang, Z. Xing, B.J. Xi, J.K. Feng, S.L. Xiong, Enhanced capacity and rate capability of nitrogen/oxygen dual-doped hard carbon in capacitive potassium-ion storage, *Adv. Mater.* 30 (2018), 1700104, <https://doi.org/10.1002/adma.201700104>.
- [22] Y.X. Chen, B.J. Xi, M. Huang, L.L. Shi, S.Z. Huang, N.N. Guo, D. Li, Z.C. Ju, S. L. Xiong, Defect-selectivity and “order-in-disorder” engineering in carbon for durable and fast potassium storage, *Adv. Mater.* 34 (2022), 2108621, <https://doi.org/10.1002/adma.202108621>.
- [23] X.A. Chen, Z.B. Xiao, X.T. Ning, Z. Liu, Z. Yang, C. Zou, S. Wang, X.H. Chen, Y. Chen, S.M. Huang, Sulfur-impregnated, sandwich-type, hybrid carbon nanosheets with hierarchical porous structure for high-performance lithium-sulfur batteries, *Adv. Energy Mater.* 4 (2014), 1301988, <https://doi.org/10.1002/aenm.201301988>.
- [24] G.Z. Cheng, W.Z. Zhang, W. Wang, H.L. Wang, Y.X. Wang, J. Shi, J.W. Chen, S. Liu, M.H. Huang, D. Mitlin, Sulfur and nitrogen codoped cyanoethyl cellulose-derived carbon with superior gravimetric and volumetric capacity for potassium ion storage, *Carbon Energy* 4 (2022) 986–1001, <https://doi.org/10.1002/cey2.233>.
- [25] W.L. Zhang, J. Ming, W.L. Zhao, X.C. Dong, M.N. Hedhili, P.M.F.J. Costa, H. N. Alshareef, Graphitic nanocarbon with engineered defects for high-performance potassium-ion battery anodes, *Adv. Funct. Mater.* 29 (2019), 1903641, <https://doi.org/10.1002/adfm.201903641>.
- [26] W.L. Wang, W.J. Li, S. Wang, Z.C. Miao, H.K. Liu, S.L. Chou, Structural design of anode materials for sodium-ion batteries, *J. Mater. Chem. A* 6 (2018) 6183–6205, <https://doi.org/10.1039/C7TA10823K>.
- [27] Z.C. Ju, P.Z. Li, G.Y. Ma, Z. Xing, Q.C. Zhuang, Y.T. Qian, Few layer nitrogen-doped graphene with highly reversible potassium storage, *Energy Storage Mater.* 11 (2018) 38–46, <https://doi.org/10.1016/j.ensm.2017.09.009>.
- [28] J.J. Zhang, H.P. Zhao, J. Li, H.L. Jin, X.C. Yu, Y. Lei, S. Wang, In situ encapsulation of iron complex nanoparticles into biomass-derived heteroatom-enriched carbon nanotubes for high-performance supercapacitors, *Adv. Energy Mater.* 9 (2019), 1803221, <https://doi.org/10.1002/aenm.201803221>.
- [29] C. Lu, Z.T. Sun, L.H. Yu, X.Y. Lian, Y.Y. Yi, J. Li, Z.F. Liu, S.X. Dou, J.Y. Sun, Enhanced kinetics harvested in heteroatom dual-doped graphitic hollow architectures toward high rate printable potassium-ion batteries, *Adv. Energy Mater.* 10 (2020), 2001161, <https://doi.org/10.1002/aenm.202001161>.
- [30] H.L. Deng, L. Wang, S.Y. Li, M. Zhang, T. Wang, J. Zhou, M.X. Chen, S. Chen, J. H. Cao, Q.S. Zhang, J. Zhu, B.A. Lu, Radial pores in nitrogen/oxygen dual-doped carbon nanospheres anode boost high-power and ultrastable potassium-ion batteries, *Adv. Funct. Mater.* 31 (2021), 2107246, <https://doi.org/10.1002/adfm.202107246>.
- [31] C. Xu, Z.T. Sun, Y. Guo, D. Luo, J. Qian, X.P. Li, Y. Wang, Multiscale hierarchically engineered carbon nanosheets derived from covalent organic framework for potassium ion battery, *Small Methods* 4 (2020), 2000159, <https://doi.org/10.1002/smt.202000159>.
- [32] J.T. Chen, B.J. Yang, H.J. Hou, H.X. Li, L. Liu, L. Zhang, X.B. Yan, Disordered, large interlayer spacing, and oxygen-rich carbon nanosheets for potassium ion hybrid capacitor, *Adv. Energy Mater.* 9 (2019), 1803894, <https://doi.org/10.1002/aenm.201803894>.
- [33] Z.L. Jian, S. Hwang, Z.F. Li, A.S. Hernandez, X.F. Wang, Z.Y. Xing, D. Su, X.L. Ji, Hard-soft composite carbon as a long-cycling and high-rate anode for potassium-ion batteries, *Adv. Funct. Mater.* 27 (2017), 1700324, <https://doi.org/10.1002/adfm.201700324>.
- [34] S.W.L. Ng, G. Yilmaz, W.L. Ong, G.W. Ho, One-step activation towards spontaneous etching of hollow and hierarchical porous carbon nanospheres for enhanced pollutant adsorption and energy storage, *Appl. Catal. B Environ.* 220 (2018) 533–541, <https://doi.org/10.1016/j.apcatb.2017.08.069>.
- [35] T. Gao, C.Y. Xu, R.Q. Li, R. Zhang, B.L. Wang, X.F. Jiang, M. Hu, Y. Bando, D. S. Kong, P.C. Dai, X.-B. Wang, Biomass-derived carbon paper to sandwich magnetite anode for long-life li-ion battery, *ACS Nano* 13 (2019) 11901–11911, <https://doi.org/10.1021/acsnano.9b05978>.
- [36] Y.R. Qi, Y.X. Lu, L.L. Liu, X.G. Qi, F.X. Ding, H. Li, X.J. Huang, L.Q. Chen, Y.-S. Hu, Retarding graphitization of soft carbon precursor: from fusion-state to solid-state carbonization, *Energy Storage Mater.* 26 (2020) 577–584, <https://doi.org/10.1016/j.ensm.2019.11.031>.
- [37] W.J. Guo, C. Geng, Z.F. Sun, J.M. Jiang, Z.C. Ju, Microstructure-controlled amorphous carbon anode via pre-oxidation engineering for superior potassium-ion storage, *J. Colloid Interface Sci.* 623 (2022) 1075–1084, <https://doi.org/10.1016/j.jcis.2022.05.073>.
- [38] H. Chen, N. Sun, Y.X. Wang, R.A. Soomro, B. Xu, One stone two birds: Pitch assisted microcrystalline regulation and defect engineering in coal-based carbon anodes for sodium-ion batteries, *Energy Storage Mater.* 56 (2023) 532–541, <https://doi.org/10.1016/j.ensm.2023.01.042>.
- [39] Z.F. Sun, Y.X. Chen, B.J. Xi, C. Geng, W.J. Guo, Q.C. Zhuang, X.G. An, J. Liu, Z. C. Ju, S.L. Xiong, Edge-oxidation-induced densification towards hybrid bulk carbon for low-voltage, reversible and fast potassium storage, *Energy Storage Mater.* 53 (2022) 482–491, <https://doi.org/10.1016/j.ensm.2022.09.031>.
- [40] H.N. He, J. He, H.B. Yu, L. Zeng, D. Luo, C.H. Zhang, Dual-interfering chemistry for soft-hard carbon translation toward fast and durable sodium storage, *Adv. Energy Mater.* 13 (2023), 2300357, <https://doi.org/10.1002/aenm.202300357>.
- [41] M.I. Kim, S.W. Seo, C.H. Kwak, J.H. Cho, J.S. Im, The effect of oxidation on the physical activation of pitch: crystal structure of carbonized pitch and textural properties of activated carbon after pitch oxidation, *Mater. Chem. Phys.* 267 (2021), 124591, <https://doi.org/10.1016/j.matchemphys.2021.124591>.
- [42] D.P. Qiu, J.Y. Guan, M. Li, C.H. Kang, J.Y. Wei, F. Wang, R. Yang, Cucurbit[6]uril-derived nitrogen-doped hierarchical porous carbon confined in graphene network for potassium-ion hybrid capacitors, *Adv. Sci.* 7 (2020), 2001681, <https://doi.org/10.1002/advs.202001681>.
- [43] Y.X. Chen, L.L. Shi, D. Li, Y. Dong, Q. Yuan, S.Z. Huang, H.Y. Yang, X.Y. Wei, Q. C. Zhuang, Z.C. Ju, H.H. Song, Undercooling-directed NaCl crystallization: an approach towards nanocavity-linked graphene networks for fast lithium and sodium storage, *Nanoscale* 12 (2020) 7622–7630, <https://doi.org/10.1039/D0NR01126F>.
- [44] Y.X. Chen, L.L. Shi, Q. Yuan, A. Li, S.Z. Huang, H.Y. Yang, X.H. Chen, J.S. Zhou, H. H. Song, Crystallization-induced morphological tuning toward denim-like graphene nanosheets in a KCl-copolymer solution, *ACS Nano* 12 (2018) 4019–4024, <https://doi.org/10.1021/acsnano.8b01708>.
- [45] M.K. Shen, H.B. Ding, L. Fan, A.M. Rao, J. Zhou, B.A. Lu, Neuromorphic carbon for fast and durable potassium storage, *Adv. Funct. Mater.* 33 (2023), 2213362, <https://doi.org/10.1002/adfm.202213362>.
- [46] Y.F. Feng, K.D. Wu, S.S. Wu, Y.Y. Guo, M. He, M. Xue, Carbon quantum dots-derived carbon nanosphere coating on Ti₃C₂ MXene as a superior anode for high-performance potassium-ion batteries, *ACS Appl. Mater. Interfaces* 15 (2023) 3077–3088, <https://doi.org/10.1021/acsaami.2c20559>.
- [47] P. Nie, M.Q. Liu, W.H. Qu, M.Q. Hou, L.M. Chang, Z.M. Wu, H.R. Wang, J.M. Jiang, Unravelling the solvation structure and interfacial mechanism of fluorinated

- localized high concentration electrolytes in K-ion batteries, *Adv. Funct. Mater.* (2023), 2302235, <https://doi.org/10.1002/adfm.202302235>.
- [48] C.X. Wang, R.H. Yu, W. Luo, W.C. Feng, Y.H. Shen, N. Xu, L.Q. Mai, Chemical cross-linking and mechanically reinforced carbon network constructed by graphene boosts potassium ion storage, *Nano Res.* 15 (2022) 9019–9025, <https://doi.org/10.1007/s12274-022-4586-x>.
- [49] B. Sun, Q. Zhang, W.L. Xu, R. Zhao, C.Z. Zhang, J.G. Guo, H. Zhu, G.M. Yuan, W. Lv, X.K. Li, N.J. Yang, Edge-enriched and S-doped carbon nanorods to accelerate electrochemical kinetics of sodium/potassium storage, *Carbon* 201 (2023) 776–784, <https://doi.org/10.1016/j.carbon.2022.09.066>.
- [50] X.Q. Ma, N. Xiao, J. Xiao, X.D. Song, H.D. Guo, Y.T. Wang, S.J. Zhao, Y.P. Zhong, J. S. Qiu, Nitrogen and phosphorus dual-doped porous carbons for high-rate potassium ion batteries, *Carbon* 179 (2021) 33–41, <https://doi.org/10.1016/j.carbon.2021.03.067>.
- [51] W.X. Yang, J.H. Zhou, S. Wang, Z.C. Wang, F. Lv, W.S. Zhang, W.Y. Zhang, Q. Sun, S.J. Guo, A three-dimensional carbon framework constructed by N/S co-doped graphene nanosheets with expanded interlayer spacing facilitates potassium ion storage, *ACS Energy Lett.* 5 (2020) 1653–1661, <https://doi.org/10.1021/acsenerylett.0c00413>.
- [52] X. Hu, Y.J. Liu, J.X. Chen, L.C. Yi, H.B. Zhan, Z.H. Wen, Fast redox kinetics in Bi-heteroatom doped 3D porous carbon nanosheets for high-performance hybrid potassium-ion battery capacitors, *Adv. Energy Mater.* 9 (2019), 1901533, <https://doi.org/10.1002/aenm.201901533>.
- [53] J.F. Ruan, F.J. Mo, Z.L. Chen, M. Liu, S.Y. Zheng, R.B. Wu, F. Fang, Y. Song, D. L. Sun, Rational construction of nitrogen-doped hierarchical dual-carbon for advanced potassium-ion hybrid capacitors, *Adv. Energy Mater.* 10 (2020), 1904045, <https://doi.org/10.1002/aenm.201904045>.
- [54] W.L. Zhang, M.L. Sun, J. Yin, K. Lu, U. Schwingschlogl, X.Q. Qiu, H.N. Alshareef, Accordion-like carbon with high nitrogen doping for fast and stable K ion storage, *Adv. Energy Mater.* 11 (2021), 2101928, <https://doi.org/10.1002/aenm.202101928>.
- [55] J.X. Hu, Y.Y. Xie, M. Yin, Z.A. Zhang, Nitrogen doping and graphitization tuning coupled hard carbon for superior potassium-ion storage, *J. Energy Chem.* 49 (2020) 327–334, <https://doi.org/10.1016/j.ijechem.2020.03.005>.
- [56] L. Tao, Y.P. Yang, H.L. Wang, Y.L. Zheng, H.C. Hao, W.P. Song, J. Shi, M.H. Huang, D. Mitlin, Sulfur-nitrogen rich carbon as stable high capacity potassium ion battery anode: performance and storage mechanisms, *Energy Storage Mater.* 27 (2020) 212–225, <https://doi.org/10.1016/j.ensm.2020.02.004>.
- [57] Y. Xu, C.L. Zhang, M. Zou, Q. Fu, C.X. Zhao, M.H. Wu, Y. Lei, Highly nitrogen doped carbon nanofibers with superior rate capability and cyclability for potassium ion batteries, *Nat. Commun.* 9 (2018) 1720, <https://doi.org/10.1038/s41467-018-04190-z>.
- [58] Y.X. Chen, L.L. Shi, S.S. Guo, Q. Yuan, X.H. Chen, J.S. Zhou, H.H. Song, A general strategy towards carbon nanosheets from triblock polymers as high-rate anode materials for lithium and sodium ion batteries, *J. Mater. Chem. A* 5 (2017) 19866–19874, <https://doi.org/10.1039/C7TA06453E>.
- [59] J.J. Wu, B. Yuan, Y.Y. Gu, Y.F. Zhang, Z.Y. Yan, L.D. Zhang, X.S. Yang, H.J. Zhang, L. Bai, Z.Q. Li, Z.-D. Huang, Multifunctional layered bismuth oxychloride/amorphous antimony oxide hetero-hybrids as superior photocatalyst and potassium ion storage materials, *Appl. Catal. B Environ.* 321 (2023), 122032, <https://doi.org/10.1016/j.apcatb.2022.122032>.
- [60] Z.L. Yu, Q. Liu, C.S. Chen, Y. Zhu, B. Zhang, Regulating the interfacial chemistry enables fast-kinetics hard carbon anodes for potassium ion batteries, *J. Power Sources* 557 (2023), 232592, <https://doi.org/10.1016/j.jpowsour.2022.232592>.
- [61] Z.L. Yu, C.S. Chen, Q. Liu, J. Liu, M.X. Tang, Y. Zhu, B. Zhang, Discovering the pore-filling of potassium ions in hard carbon anodes: Revisit the low-voltage region, *Energy Storage Mater.* 60 (2023), 102805, <https://doi.org/10.1016/j.ensm.2023.102805>.
- [62] L. Zhong, W.L. Zhang, S.R. Sun, L. Zhao, W.B. Jian, X. He, Z.Y. Xing, Z.X. Shi, Y. N. Chen, H.N. Alshareef, X.Q. Qiu, Engineering of the crystalline lattice of hard carbon anodes toward practical potassium-ion batteries, *Adv. Funct. Mater.* 33 (2023), 2211872, <https://doi.org/10.1002/adfm.202211872>.
- [63] J.M. Ge, B. Wang, J. Zhou, S.Q. Liang, A.M. Rao, B.A. Lu, Hierarchically structured nitrogen-doped carbon microspheres for advanced potassium ion batteries, *ACS Mater. Lett.* 2 (2020) 853–860, <https://doi.org/10.1021/acsmaterialslett.0c00171>.
- [64] K.-T. Chen, H.-Y. Tuan, Bi–Sb nanocrystals embedded in phosphorus as high-performance potassium ion battery electrodes, *ACS Nano* 14 (2020) 11648–11661, <https://doi.org/10.1021/acsnano.0c04203>.
- [65] M.T. Cai, H.H. Zhang, Y.G. Zhang, B.S. Xiao, L. Wang, M. Li, Y. Wu, B.S. Sa, H. G. Liao, L. Zhang, S.Q. Chen, D.-L. Peng, M.-S. Wang, Q.B. Zhang, Boosting the potassium-ion storage performance enabled by engineering of hierarchical MoSSe nanosheets modified with carbon on porous carbon sphere, *Sci. Bull.* 67 (2022) 933–945, <https://doi.org/10.1016/j.scib.2022.02.007>.
- [66] Y.H. Xie, Y. Chen, L. Liu, P. Tao, M.P. Fan, N. Xu, X.W. Shen, C.L. Yan, Ultra-high pyridinic N-doped porous carbon monolith enabling high-capacity K-ion battery anodes for both half-cell and full-cell applications, *Adv. Mater.* 29 (2017), 1702268, <https://doi.org/10.1002/adma.201702268>.
- [67] H.J. Kim, J.H. Jo, J.U. Choi, N. Voronina, D. Ahn, T.-Y. Jeon, H. Yashiro, Y. Anishevich, G. Ragoisha, E. Streltsov, S.-T. Myung, Long life anode material for potassium ion batteries with high-rate potassium storage, *Energy Storage Mater.* 40 (2021) 197–208, <https://doi.org/10.1016/j.ensm.2021.05.012>.
- [68] B. Wang, L. Gu, F. Yuan, D. Zhang, H.L. Sun, J. Wang, Q.J. Wang, H. Wang, Z.J. Li, Edge-enrich N-doped graphitic carbon: Boosting rate capability and cyclability for potassium ion battery, *Chem. Eng. J.* 432 (2022), 134321, <https://doi.org/10.1016/j.cej.2021.134321>.
- [69] L. Li, Z. Hu, Y. Lu, C.C. Wang, Q. Zhang, S. Zhao, J. Peng, K. Zhang, S.-L. Chou, J. Chen, A low-strain potassium-rich prussian blue analogue cathode for high power potassium-ion batteries, *Angew. Chem. Int. Ed.* 60 (2021) 13050–13056, <https://doi.org/10.1002/anie.202103475>.